



Ensuring the possibility of using thorium as a fuel in a pressurized water reactor (PWR)

Mohamed Y. M. Mohsen¹ · Mohamed A. E. Abdel-Rahman¹ ·
A. Abdelghafar Galahom²

Received: 28 September 2021 / Revised: 2 November 2021 / Accepted: 6 November 2021 / Published online: 10 December 2021
© The Author(s), under exclusive licence to China Science Publishing & Media Ltd. (Science Press), Shanghai Institute of Applied Physics, the Chinese Academy of Sciences, Chinese Nuclear Society 2021

Abstract The possibility of utilizing thorium as a fuel in a pressurized water reactor (PWR) has been proven from the neutronic perspective in our previously published work without assessing the thermal hydraulic (TH) and solid structure performances. Therefore, the TH and solid structure performances must be studied to confirm these results and ensure the possibility of using a thorium-based fuel as an excellent accident-tolerant fuel. The TH and solid structure performances of thorium-based fuels were investigated and compared with those of UO_2 . The radial and axial power peaking factors (PPFs) for UO_2 , (^{232}Th , ^{235}U) O_2 , and (^{232}Th , ^{233}U) O_2 were examined with a PWR assembly to determine the total PPF of each one. Both Gd_2O_3 and Er_2O_3 were tested as burnable absorbers (BAs) to manage the excess reactivity at the beginning of the fuel cycle (BOC) and reduce the total PPF. Er_2O_3 resulted in a more significant reduction to the total PPF and, therefore, a greater reduction to the temperature distribution compared to Gd_2O_3 . Given these results, we analyzed the effects of adding Er_2O_3 to thorium-based fuels on their TH and solid structure performances.

Keywords Thermal hydraulic (TH) · Solid structure · Thorium-based fuel · Gd_2O_3 · Er_2O_3

1 Introduction

Since the nuclear accident of Fukushima Daiichi, many efforts have been made to find an accident-tolerant fuel (ATF) that can safely operate under harsh conditions inside the reactor. This type of fuel would prevent the reactor core from melting down and causing a disaster [1, 2]. ATFs must have better properties than traditional fuels to perform essential tasks during accident conditions, for example, decreasing oxidation kinetics and hydrogen generation rates.

Thorium-based fuels have advantages that invite researchers to investigate the possibility of using them as AFTs, such as their high resistance to nuclear proliferation and the low quantity of long-lived minor actinides (MAs) and non-actinides in the discharged fuel from the reactor [3–8]. Various forms of thorium-based fuels have been certified, such as oxides, metals, nitrides, carbides, and molten salts. These fuels have also been nominated as nuclear fuels for different types of reactors, including heavy-water reactors, light-water reactors, accelerator-driven systems, and high-temperature gas-cooled reactors. The breeding capability of Th-U fuel material in accelerator-driven subcritical molten salt reactors has already been studied, where researchers determined the conversion ratio and net production of ^{233}U and the inventories of the various MAs [9].

Thorium dioxide carries significant research interest as an alternative to the traditional fuel material of uranium dioxide in Generation IV reactors due to many reasons, including its high abundance in the earth's crust, its effectiveness in power flattening for nuclear reactors, its usefulness as a breeder blanket to generate ^{233}U , and its capability to suppress neutron leakage from the reactor

✉ A. Abdelghafar Galahom
Agalahom@yahoo.com; Galhom_20102000@yahoo.com

¹ Nuclear Engineering Department, Military Technical College, Kobry Elkobbah, Cairo, Egypt

² Higher Technological Institute, 10th of Ramadan City, Egypt

core [5, 10, 11]. This interest also comes from its physical advantages, such as its high melting point, high corrosion resistivity, low thermal expansion coefficients, and high thermal conductivity, compared to traditional fuel materials [4, 12, 13]. Moreover, the fission gas release is lower than in uranium dioxide, which keeps the fuel pellet away from any defects that could have side effects on the TH and solid structure performances. These advantages provide the fuel material with greater stability during severe operational conditions from the neutronic, TH, and solid structure viewpoints. Spark plasma sintering (SPS) is an example of the technologies used to produce high-density (^{232}Th , U) O_2 pellets, in which electric current flows through the sample and a conductive die provides rapid sintering and low temperatures [2].

Thorium dioxide has a melting point of 3651 K and is used as a ceramic fuel pellet in nuclear reactors. Its melting point is the highest known melting point for an oxide. Thorium dioxide also has an identical fluorite structure to cerium, plutonium, and uranium dioxide. However, thorium dioxide has a higher oxidation state than uranium and plutonium dioxides, making it exceptionally stable in the presence of oxygen or water and boosting its corrosion resistance [14]. The existence of uranium in thorium dioxide can occur in two ways: either, through the doping process, in which, uranium is added to the thorium in a mixed oxide fuel (MOX); or, through the transmutation of the ^{232}Th isotope into the fissile ^{233}U isotope by bombarding it with a neutron, resulting in two successive beta emissions [13].

This study has three primary sections. In the first section, we investigate and compare the TH and solid structure performances of the suggested thorium-based fuel types with those of traditional fuels; then, in the second section, we determine which of the two different burnable absorbers (BAs) (Gd_2O_3 and Er_2O_3) added to the standard fuel was most suitable; and lastly, in the third section, we investigate the optimum BA for thorium-based fuel.

2 Methodology

Version 2.7 of the Monte Carlo N-Particle transport code system (MCNPX) was used with a cross-section library called ENDF/B-VII to design a three-dimensional model of the PWR fuel assembly (FA). The MCNPX code, based on the Monte Carlo method, is a multi-purpose code that can simulate almost all particles in the PWR environment. It was used to investigate the radial power distribution and specify the hot channel where the TH and solid structure analyses would be performed [15, 16]. Figure 1 illustrates the horizontal cross-section assembly model of the PWR, as generated by MCNPX. In total, 70

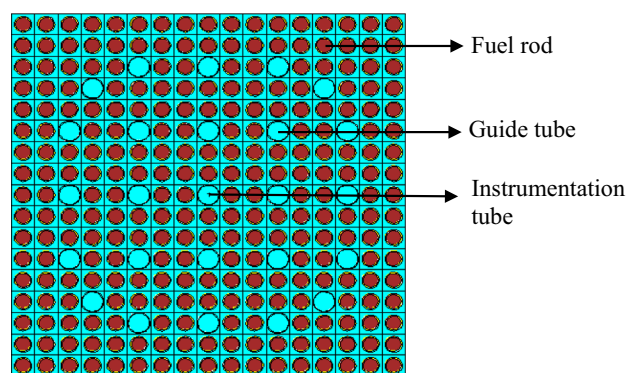


Fig. 1 (Color online) Horizontal cross section of the PWR FA using visual editor version X_24E of MCNPX

000 histories per cycle, 20 ineffective cycles, and 100 effective cycles were used in the neutronic computations. The boundary surfaces of the fuel assembly are reflection surfaces that reflect the neutrons inside the fuel assembly. The calculations were carried out under hot full-power conditions (HFP).

The COMSOL Multiphysics computer software, which is dependent on the computational fluid dynamics (CFD) technique, was applied to investigate the TH and solid structure performances. The rod-centered subchannel model was utilized and solved numerically in the TH study. The temperature distribution for the fuel, cladding, and coolant materials, the coolant pressure drop, and the departure from nucleate boiling ratio (DNBR) was investigated using the rod-centered subchannel model. The most prominent advantage of the CFD approach is the coupling of various types of physics, which makes the solution more realistic than the analytical approach. The coupling of heat transfer and turbulence (K - ϵ) physics mimics the effects of coolant velocity fluctuation in the axial and radial directions, and therefore, the variation of the coolant heat transfer convection coefficient, on the temperature distribution of the fuel and cladding materials. For these reasons, we used this coupling to perform our TH analysis. The coupling of solid structure and heat transfer physics helps to investigate the effects of the thermal expansion of solid materials (fuel and cladding) on von Mises stress and total displacement. To simulate the effect of the coolant pressure on the solid materials, the turbulence and solid structure physics coupling was considered. We used the 2D axisymmetric space dimension, rather than the 3D space dimension, to simulate the TH and solid structure for the hot channel in each FA to simplify the simulation and reduce the calculation time and cost. To calculate the distribution of the DNBR, the EPRI-1 correlation for PWR was used [18]; this process has been illustrated in detail in our previously published article [17]. Table 1 lists the properties of the examined fuel types. In this work, the TH

Table 1 Characteristics of the examined ATFs

Fuel type	Enrichment (wt%)	Density (g/cm ³)
UO ₂	3.5	10.32
(²³² Th, ²³⁵ U) O ₂		9.64
(²³² Th, ²³³ U) O ₂		9.5

and solid structure performances of UO₂ were investigated and compared with the thorium-based fuel types. Table 2 shows the main design features and input data used for simulating the TH and solid structure performances using COMSOL Multiphysics. Table 3 presents the correlations that describe the thermophysical and solid structure properties of the applied materials.

3 Results and discussion

The TH and solid structure performances were investigated to provide an integrated study on the effectiveness of using (²³²Th, ²³⁵U)O₂ and (²³²Th, ²³³U)O₂ as nuclear fuels in the PWR. Performances in TH and solid structures have been investigated at the HFP near the BOC. This state is characterized by a higher PPF relative to the PPF value during the rest of the fuel cycle. This is true because the PPF decreases as the fuel burn-up increases. The TH and solid structure performances of (²³²Th, ²³⁵U)O₂ and (²³²Th, ²³³U)O₂, without burnable absorbers, will be discussed and compared with UO₂ in the following section.

3.1 Comparing thorium-based fuel with UO₂ without a burnable absorber

The TH and solid structure performances of (²³²Th, ²³⁵U)O₂ and (²³²Th, ²³³U)O₂ were investigated and compared with those of UO₂. To study the TH and solid structure of the proposed fuel types, it is important to analyze the radial and axial power distributions through the

Table 2 TH and solid structure main design features

Parameters	Value
Inlet coolant pressure (MPa)	15.41
Inlet coolant temperature (K)	562.15
Coolant mass flow rate (kg/s)	16,720
Core thermal power (MW _{th})	3358
Critical flux	EPRI-1 correlation [15]
Wall condition	No-slip
Turbulence model	<i>K</i> - ϵ

FA. The power distribution was determined using the MCNPX code. Figure 2 presents the radial and axial PPF distributions of the investigated fuel types, with the hot channels where the power is peaking marked by orange cells. The total PPF is calculated from the axial and radial PPFs using Eq. (1).

$$\text{Total PPF} = \text{Radial PPF} \times \text{Axial PPF} \times \text{channel factor} [23]. \quad (1)$$

Table 4 lists the radial, axial, and total PPF for the investigated fuel types. It is observed that the total PPF in the case of (²³²Th, ²³³U) O₂ is smaller than that of the other fuel materials studied. This is because the infinite multiplication factor (K_{inf}) at the HFP and the beginning of the fuel cycle length for (²³²Th, ²³³U) O₂ is greater than that of the other investigated fuel assemblies [3]. The normalization factor used in the multiplier card in the tallies (FM) is inversely proportional to the K_{inf} for the same thermal power. Therefore, to produce almost the same thermal power from the three investigated fuel assemblies, the normalization factor for both the flux and power for (²³²Th, ²³³U) O₂ is smaller than that of the other fuel materials studied.

3.1.1 Thermal–hydraulic performance

The subchannel model based on the CFD technique was used to solve the equations of the coupled system (partial differential heat generation equation for heat transfer and Navier–Stokes equation for fluid dynamics). The rod-centered subchannel model is discussed in detail in our previously published work [18]. The primary goal of the TH analysis was to obtain the DNBR distribution and the temperature distribution of the coolant, clad, and fuel. Figure 3 presents the temperature distribution of the coolant, cladding, and fuel materials, where the maximum fuel temperatures for the examined FAs of UO₂, (²³²Th, ²³⁵U)O₂, and (²³²Th, ²³³U)O₂ are 1565.21 K, 1497.56 K, and 1403.49 K, respectively. The safety limits for the fuel temperatures are less than 2873 K for UO₂ and 3500 K for (U, Th) O₂, which ensures safe operation and the impossibility of fuel meltdown at the BOC. For the maximum clad inner surface temperature, the UO₂ FA had a maximum temperature of 611.859 K, while for the thorium-based fuels, the maximum temperatures were 610.29 K for (²³²Th, ²³⁵U)O₂ and 606.18 K for (²³²Th, ²³³U)O₂. Additionally, the maximum clad temperatures indicate that the clad material meltdown is impossible because the maximum clad temperatures are less than 2123 K, the melting point of zircaloy-4. Furthermore, these temperatures ensure the impossibility of the pellet cladding chemical interactions (PCCI) because they are less than 1135 K. The EPRI-

Table 3 Correlations used for describing the thermophysical and solid structure properties for the applied materials

Thermophysical property	Applied correlation
UO_2	
$K_{0.95} \left[\frac{W}{(cmK)} \right]$	$\frac{1}{A+Bt} + \frac{E}{T^2} e^{-\frac{F}{T}}$ [17]
$Cp \left[\frac{J}{(moleK)} \right]$	$c_2 + 2c_3t + 3c_4t^2 + 4c_5t^3 + 5c_6t^4 - c_7t^{-2}$ [17]
$\rho \left[\frac{kg}{m^3} \right]$	$\rho(T) = \rho_o \times (K_i)^{-3}$ [19]
	$K_i = 0.9967 + 1.179 \times 10^{-5} \times T - 2.429 \times 10^{-9} \times T^2 + 1.2190 \times 10^{-12} \times T^3$
E (GPa)	$\rho_o(273) = 10.961 \text{ g/cm}^3$ $(217.24 \pm 4.01)(1 - 1.92 \times P)$ [20] P is the porosity
ν	$\left(1.323 \times \left[\frac{(1-1.92 \times P)}{(1-1.66 \times P)} \right] - 1 \right)$ [20] P is the porosity
$\alpha \left[\frac{1}{K} \right]$	$\frac{\alpha(T)}{\alpha(273)} = 0.9973 + 9.802 \times 10^{-6}T - 2.705 \times 10^{-10}T^2 + 4.219 \times 10^{-13}T^3$
	For $323 < T < 923$ K
	$\frac{\alpha(T)}{\alpha(273)} = 0.9967 + 1.179 \times 10^{-5}T - 2.429 \times 10^{-9}T^2 + 1.219 \times 10^{-12}T^3$
	For $923 < T < 3120$ K
	$\alpha(273)$ equal to 9.75×10^{-6} [19]
(Zircaloy-4)	
$K \left[\frac{W}{(mK)} \right]$	$23.5 - 0.0192 \times T + 1.86 \times 10^{-5} \times T^2$ [19]
$Cp \left[\frac{J}{(kgK)} \right]$	$238 + 0.159T$ [19]
$\rho \left[\frac{kg}{m^3} \right]$	$6650 - 0.286T$ [19]
E (Pa)	$9.21 \times 10^{10} - 4.05 \times 10^7 \times T$ [21]
ν	0.37
$\alpha \left[\frac{1}{K} \right]$	$(5.22 + 1.82 \times 10^{-3}T) \times 10^{-6}$ [19]
(U, Th) O ₂	
$K \left[\frac{W}{(mK)} \right]$	$14.242 - 0.022T + 1.764 \times 10^{-5}T^2 - 6.380 \times 10^{-9}T^3 + 8.038 \times 10^{-13}T^4$ [6]
$Cp \left[\frac{J}{(moleK)} \right]$	$239.9 + 8.512 \times 10^{-5}T - 5.754 \times 10^{-8}T^2 + 1.528 \times 10^{-11}T^3$ [22]
$\rho \left[\frac{kg}{m^3} \right]$	$9326 - 0.0004T + 2.54 \times 10^{-7}T^2 - 7.897 \times 10^{-11}T^3$ [22]
E [Pa]	$259.87 \times 10^9 \times (1 - P^2)$ [6] P is the porosity
ν	0.36

Table 3 continued

Thermophysical property	Applied correlation
$\alpha \left[\frac{1}{\text{K}} \right]$	$5.416 \times 10^{-6} + 3.747 \times 10^{-9}T + 3.0107 \times 10^{-15}T^2 - 1.2212 \times 10^{-15}T^3 + 4.181 \times 10^{-19}T^4$ [14]
Water (compressed liquid) and helium (gas)	
Their thermophysical properties exist in the material library of COMSOL Multiphysics	

1 correlation was utilized to determine the critical heat flux (CHF), which was divided by the actual heat flux to calculate the DNBR. The DNBR was then studied to explain how far the coolant is from the nucleate boiling hazards by comparing the minimum DNBR with the PWR's safety margin of 1.75. The minimum DNBR values were 1.767, 1.765, and 1.8615 for UO_2 , $(^{232}\text{Th}, ^{235}\text{U})\text{O}_2$, and $(^{232}\text{Th}, ^{233}\text{U})\text{O}_2$, respectively, which emphasizes that the formulation of nucleate boiling is impossible. It can be noticed that the temperature distributions of the investigated fuel materials are similar. This is primarily because the values of thermal conductivity for the UO_2 and the two suggested thorium-based fuels are almost equal, as shown in Table 3. However, the thorium-based fuels show a safe performance relative to that of UO_2 because of their higher melting points compared to those of the traditional fuel. There are various types of temperature changes with radius within the radial temperature distribution, where it is parabolic ($1/r^2$) across the fuel materials. Furthermore, in both the He gap and clad materials, the temperature changes exponentially ($\ln(1/r)$). Finally, in the coolant material, the temperature changes with $1/r$. Figure 4 presents the distributions of the temperature along the channels that have the maximum PPF inside the fuel types under examination.

3.1.2 Solid structure performance

In this section, the primary solid structure parameters (von Mises stress and the displacement of the outer fuel surface) were simulated. The von Mises stress is the total stress that affects the materials and is caused by either thermal or pressure loads. The thermal loads are due to the fission energy that is transferred to the coolant through the fuel and clad materials, which causes thermal expansion. The pressure loads were caused by the coolant pressure. If the von Mises stress is larger than the yield stress, the fuel material transfers from the elastic zone to the plastic or ductile zone. Therefore, for safe operation, the von Mises stress should not exceed the yield stress. The possibility of

PCCI can be determined from the displacement of the fuel outer surface. The main causes of PCCI are the temperature of the clad materials reaching 1135, and the surfaces of both fuel and clad materials coming into contact. Under these conditions, the uranium atoms interact chemically with the zirconium atoms to form PCCI. Another type of interaction between the fuel and clad materials is called pellet clad mechanical interaction (PCMI). This type of interaction occurs when the outer surface of the fuel pellets expands thermally to reach the surface of the clad materials, resulting in excessive compression stress on the clad material, or where the clad exerts excess compression stress on the fuel material owing to its thermal expansion. Figure 5 shows that the highest von Mises pressures occurring on the investigated FAs of UO_2 , $(^{232}\text{Th}, ^{235}\text{U})\text{O}_2$, and $(^{232}\text{Th}, ^{233}\text{U})\text{O}_2$ were 144.42, 111.06, and 103.08 MPa, respectively. The displacements of the fuel's outer surface for the examined FAs of UO_2 , $(^{232}\text{Th}, ^{235}\text{U})\text{O}_2$, and $(^{232}\text{Th}, ^{233}\text{U})\text{O}_2$ were 0.145, 0.098, and 0.089 mm, respectively. Although the displacements of the fuel's outer surface for the examined fuel materials were greater than the thickness of the He gap, the occurrence of the PCCI is impossible because the maximum clad temperatures in the aforementioned fuel materials were less than 1135 K. The obtained solid structure results show a remarkable superiority of the two thorium-based fuel over the traditional UO_2 fuel material: The thermal expansion coefficient for the thorium-based fuel is lower than that for the traditional fuel material UO_2 , which reduces the thermal stress occurring on the fuel materials and decreases the displacement of the fuel's outer surface. Because of the excess reactivity at the BOC that occurred in the investigated FAs of UO_2 , $(^{232}\text{Th}, ^{235}\text{U})\text{O}_2$, and $(^{232}\text{Th}, ^{233}\text{U})\text{O}_2$, it is important to use BAs to reduce this excess reactivity. Therefore, two BAs are investigated in the following section to distinguish which is more suitable from the TH and solid structure viewpoints.

9	18		33	42		57	66	
1.022	1.077		1.122	1.128		1.132	1.122	
8	17	25	32	41	48	56	65	72
1.020	1.048	1.100	1.084	1.090	1.125	1.093	1.097	1.123
7	16	24	31	40	47	55	64	71
1.025	1.049	1.104	1.094	1.089	1.133	1.091	1.094	1.127
6	15		30	39		54	63	
1.029	1.075		1.140	1.139		1.136	1.129	
5	14	23	29	38	46	53	62	70
1.000	1.033	1.120	1.136	1.112	1.134	1.096	1.092	1.117
4	13	22		37	45	52	61	69
0.986	1.013	1.084		1.140	1.137	1.088	1.080	1.113
3	12	21	28	36		51	60	
0.972	0.987	1.029	1.085	1.114		1.105	1.101	
2	11	20	27	35	44	50	59	68
0.959	0.962	0.962	1.005	1.037	1.080	1.054	1.054	1.073
1	10	19	26	34	43	49	58	67
0.949	0.954	0.969	0.990	1.002	1.020	1.020	1.020	1.013

UO₂

9	18		33	42		57	66	
1.026	1.100		1.127	1.134		1.145	1.134	
8	17	25	32	41	48	56	65	72
1.014	1.056	1.121	1.092	1.096	1.135	1.095	1.102	1.137
7	16	24	31	40	47	55	64	71
1.026	1.064	1.121	1.094	1.112	1.139	1.105	1.087	1.134
6	15		30	39		54	63	
1.015	1.083		1.154	1.144		1.150	1.134	
5	14	23	29	38	46	53	62	70
1.016	1.055	1.132	1.159	1.130	1.150	1.093	1.097	1.144
4	13	22		37	45	52	61	69
0.991	1.022	1.109		1.153	1.147	1.087	1.087	1.122
3	12	21	28	36		51	60	
0.968	1.004	1.034	1.095	1.138		1.114	1.111	
2	11	20	27	35	44	50	59	68
0.960	0.978	0.994	1.018	1.048	1.089	1.055	1.058	1.089
1	10	19	26	34	43	49	58	67
0.951	0.955	0.979	0.986	1.006	1.016	1.014	1.025	1.032

(²³²Th,²³⁵U) O₂

9	18		33	42		57	66	
1.006	1.058		1.093	1.092		1.098	1.090	
8	17	25	32	41	48	56	65	72
0.998	1.030	1.077	1.059	1.066	1.100	1.059	1.064	1.090
7	16	24	31	40	47	55	64	71
0.985	1.028	1.082	1.064	1.065	1.100	1.072	1.065	1.096
6	15		30	39		54	63	
0.979	1.055		1.107	1.118		1.101	1.093	
5	14	23	29	38	46	53	62	70
0.957	1.017	1.082	1.113	1.085	1.106	1.066	1.065	1.095
4	13	22		37	45	52	61	69
0.952	0.990	1.060		1.106	1.097	1.066	1.058	1.085
3	12	21	28	36		51	60	
0.968	0.972	1.004	1.060	1.085		1.074	1.076	
2	11	20	27	35	44	50	59	68
0.942	0.951	0.971	0.994	1.013	1.054	1.023	1.027	1.048
1	10	19	26	34	43	49	58	67
0.934	0.949	0.949	0.971	0.984	0.994	0.987	0.993	0.996

(²³²Th,²³³U) O₂

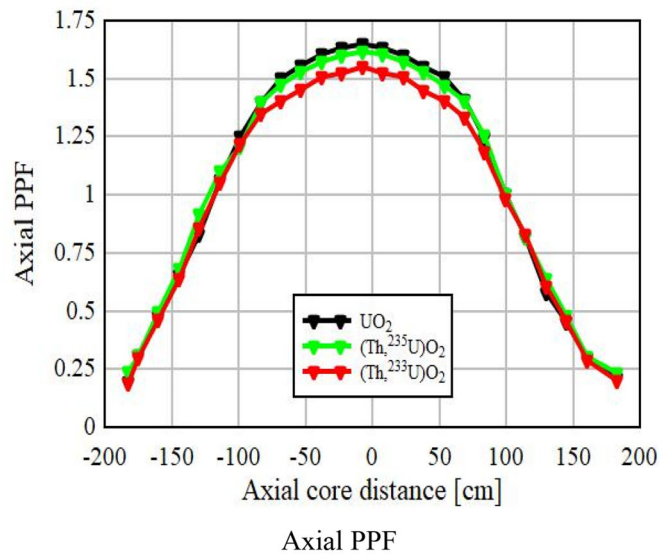


Fig. 2 (Color online) Radial and axial PPF distributions for the examined fuel assemblies (FAs)

Table 4 Radial PPF, axial PPF, and the total PPF for the investigated FAs

FA	FA with UO ₂	FA with (²³² Th, ²³⁵ U)O ₂	FA with (²³² Th, ²³³ U)O ₂
Radial PPF	1.140	1.159	1.113
Axial PPF	1.650	1.625	1.550
Total PPF	1.692	1.695	1.552

3.2 Determination of the most suitable IFBA

The main goal of utilizing the BA is to suppress the excess reactivity at the BOC. This section aims to determine the most suitable integral fuel burnable absorber

(IFBA) material to be applied to the investigated fuel types in an attempt to enhance their performance in both TH and solid structures, in addition to achieving suitable reactivity management. Both Er₂O₃ and Gd₂O₃ at a concentration of 2% were mixed with UO₂. The IFBA rods are marked in

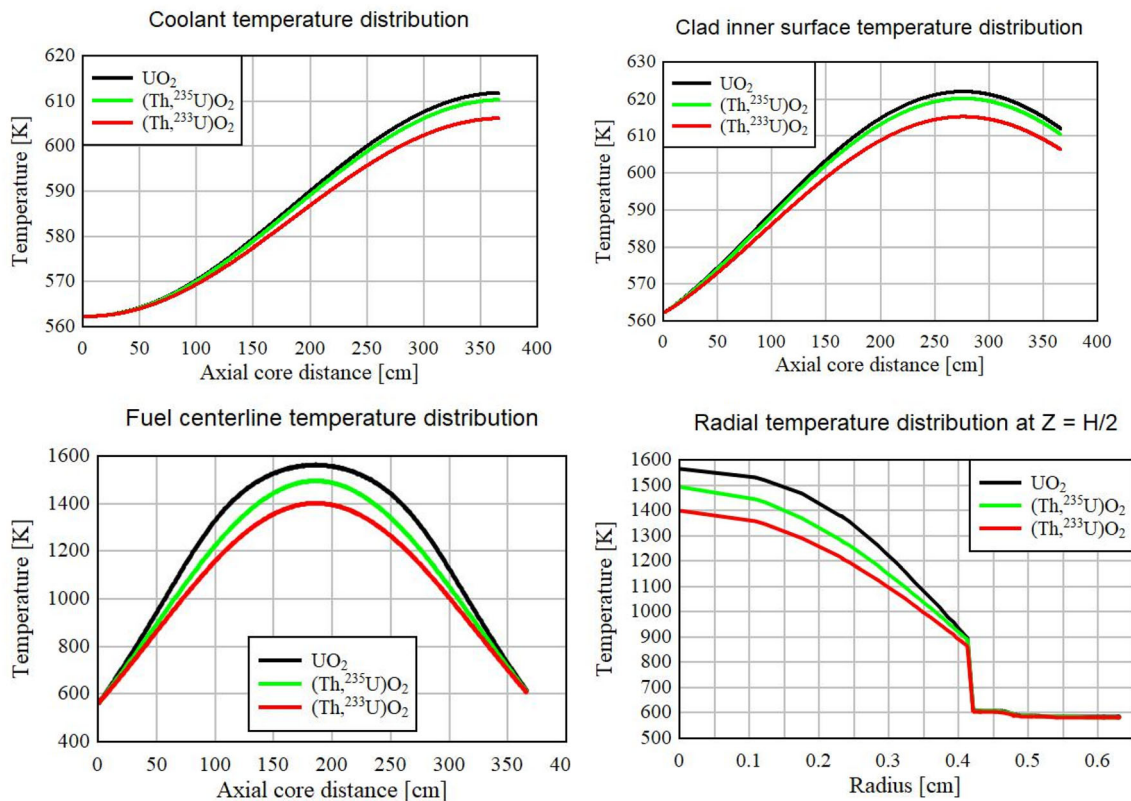


Fig. 3 (Color online) Axial and radial temperature distributions along the channels that have the maximum PPF inside the fuel types under examination

this work by the green cells in the FA. As shown in Fig. 6, the IFBAs were distributed near the guide tubes (coolant channels), where they occupied positions near the regions with the highest probability of neutron moderation, the highest probability of fission reactions, and hence the highest excess reactivity. The main goal of this distribution is to reduce the excess reactivity in this region and achieve fine-tuning of the power distribution across the FA. This is what happened after the use of $(\text{UO}_2 + \text{Er}_2\text{O}_3)$, where the total PPF decreased from 1.692 for UO_2 (without BAs) to 1.571 and the power distribution became flatter. In contrast, after the use of $(\text{UO}_2 + \text{Gd}_2\text{O}_3)$, the total PPF increased from 1.692 to 2.116. This is due to the large thermal neutron absorption cross section (49,000 barn) [24]. The three examined FAs were designed to produce nearly the same average thermal power. Therefore, the significant decrease in the power values of the IFBA rods in the case of $(\text{UO}_2 + \text{Er}_2\text{O}_3)$ was compensated by increasing the power values at the periphery of the FA.

Table 5 presents the maximum PPF in both the axial and radial directions and the total PPF for UO_2 with and without IFBAs. The total PPF in the case of UO_2 without IFBAs was 1.692. This value increases to 2.116 when Gd_2O_3 is used. The opposite occurred after applying Er_2O_3 , where the total PPF was reduced to 1.571. Therefore, the

use of Er_2O_3 not only reduces excess reactivity at the BOC, as proved in the first annex of this paper [3], but also decreases the total PPF and fine-tunes the power density distribution, which enhances the TH and solid structure performance.

3.2.1 Thermal hydraulic performance

Figure 7 presents the results of the main TH parameters, where the maximum fuel temperatures for assemblies fueled with UO_2 , $(\text{UO}_2 + \text{Er}_2\text{O}_3)$, and $(\text{UO}_2 + \text{Gd}_2\text{O}_3)$ were 1646.67 K, 1585.64 K, and 1760.87 K, respectively. The maximum clad temperatures for the three investigated FAs of UO_2 , $(\text{UO}_2 + \text{Er}_2\text{O}_3)$, and $(\text{UO}_2 + \text{Gd}_2\text{O}_3)$ were 629.46 K, 623.77 K, and 643.25 K, respectively. The MDNBR values for the FAs of UO_2 , $(\text{UO}_2 + \text{Er}_2\text{O}_3)$, and $(\text{UO}_2 + \text{Gd}_2\text{O}_3)$ were 1.767, 1.847, and 1.530, respectively. In the case of using Gd_2O_3 , the MDNBR value is lower than 1.75, which is the safety limit for the MDNBR according to the EPRI-1 correlation. Figure 8 displays the temperature distributions in 3D, where the temperature is maximum at the center of the fuel rod and decreases in the direction of the coolant. The results of the TH parameters indicate that the use of Er_2O_3 decreases the total PPF, which reduces the maximum fuel and clad temperatures

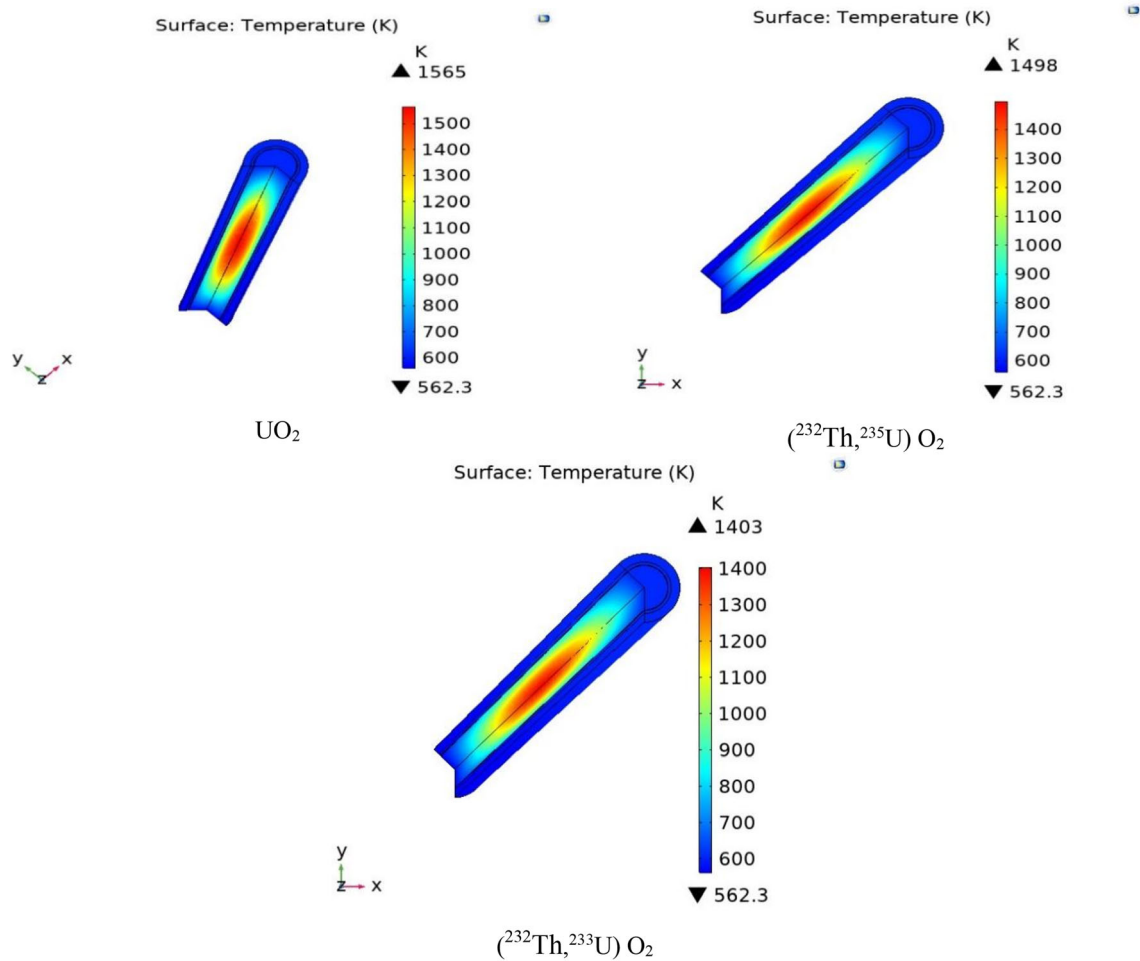


Fig. 4 (Color online) 3D temperature distribution along the channels that have the maximum PPF inside the fuel types under examination

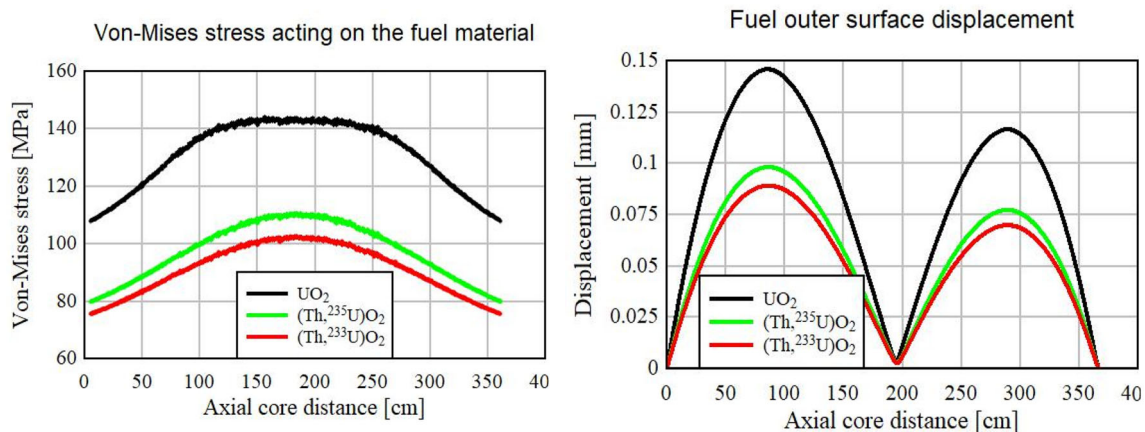


Fig. 5 (Color online) Results of the primary solid structure parameters for hot channels in the investigated FAs of UO_2 , $(^{232}\text{Th}, ^{235}\text{U})\text{O}_2$, and $(^{232}\text{Th}, ^{233}\text{U})\text{O}_2$

and increases the DNBR safety margin. Therefore, the use of Er_2O_3 led to a more significant improvement in the thermal hydraulic performance than using Gd_2O_3 .

3.2.2 Solid structure performance

Figure 9 illustrates the variation in the main solid structure parameters (the von Mises stress operating on the

9	18		33	42		57	66	
1.022	1.077		1.122	1.128		1.132	1.122	
8	17	25	32	41	48	56	65	72
1.020	1.048	1.100	1.084	1.090	1.125	1.093	1.097	1.123
7	16	24	31	40	47	55	64	71
1.025	1.049	1.104	1.094	1.089	1.133	1.091	1.094	1.127
6	15		30	39		54	63	
1.029	1.075		1.140	1.139		1.136	1.129	
5	14	23	29	38	46	53	62	70
1.000	1.033	1.120	1.136	1.112	1.134	1.096	1.092	1.117
4	13	22		37	45	52	61	69
0.986	1.013	1.084		1.140	1.137	1.088	1.080	1.113
3	12	21	28	36		51	60	
0.972	0.987	1.029	1.085	1.114		1.105	1.101	
2	11	20	27	35	44	50	59	68
0.959	0.962	0.962	1.005	1.037	1.080	1.054	1.054	1.073
1	10	19	26	34	43	49	58	67
0.949	0.954	0.969	0.990	1.002	1.020	1.020	1.020	1.013

UO₂

9	18		33	42		57	66	
1.047	1.081		1.080	1.104		0.901	1.085	
8	17	25	32	41	48	56	65	72
1.033	1.031	0.889	1.033	1.052	1.100	1.056	1.057	1.084
7	16	24	31	40	47	55	64	71
1.046	1.061	1.079	1.043	0.880	1.095	1.071	1.053	0.899
6	15		30	39		54	63	
1.058	1.099		1.112	1.106		1.086	1.086	
5	14	23	29	38	46	53	62	70
1.053	1.056	0.918	1.125	1.113	1.097	0.877	1.037	1.094
4	13	22		37	45	52	61	69
1.054	1.061	1.100		1.113	1.104	1.033	1.036	1.076
3	12	21	28	36		51	60	
1.042	1.049	1.073	1.096	0.926		1.072	0.890	
2	11	20	27	35	44	50	59	68
1.040	1.049	1.052	1.060	1.052	1.100	1.061	1.043	1.077
1	10	19	26	34	43	49	58	67
1.042	1.048	1.049	1.055	1.046	1.065	1.039	1.042	1.047

UO₂+Er₂O₃

9	18		33	42		57	66	
1.138	1.109		1.065	1.105		0.349	1.060	
8	17	25	32	41	48	56	65	72
1.139	1.071	0.354	1.000	1.016	1.102	1.020	1.057	1.058
7	16	24	31	40	47	55	64	71
1.156	1.125	1.075	1.009	0.350	1.073	1.077	1.024	0.348
6	15		30	39		54	63	
1.192	1.185		1.136	1.107		1.083	1.085	
5	14	23	29	38	46	53	62	70
1.176	1.114	0.365	1.137	1.146	1.113	0.349	1.018	1.110
4	13	22		37	45	52	61	69
1.206	1.171	1.152		1.139	1.134	1.025	1.008	1.071
3	12	21	28	36		51	60	
1.214	1.215	1.193	1.145	0.362		1.085	0.355	
2	11	20	27	35	44	50	59	68
1.220	1.213	1.200	1.162	1.107	1.184	1.139	1.068	1.115
1	10	19	26	34	43	49	58	67
1.234	1.238	1.204	1.193	1.169	1.178	1.163	1.139	1.146

UO₂+Gd₂O₃

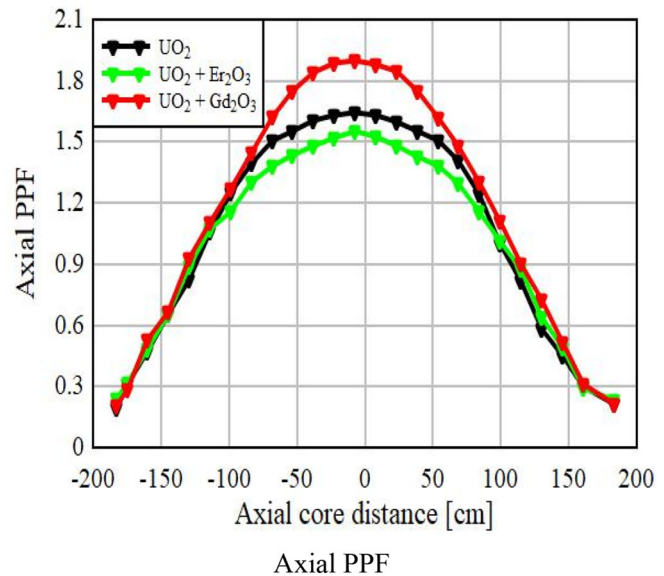


Fig. 6 (Color online) Radial and axial PPF distributions for UO₂, (UO₂ + Gd₂O₃), and (UO₂ + Er₂O₃)

Table 5 Maximum radial PPF, axial PPF, and the total PPF for the investigated FAs ((UO₂ + Gd₂O₃) and (UO₂ + Er₂O₃))

Assembly	FA with (UO ₂ + Gd ₂ O ₃)	FA with (UO ₂ + Er ₂ O ₃)
Max radial PPF	1.238	1.125
Max axial PPF	1.900	1.552
Total PPF	2.116	1.571

fuel material and the displacement of the fuel outer surface) along the axial direction. The greatest von Mises stresses operating on the fuel materials of UO₂, (UO₂ + Er₂O₃), and (UO₂ + Gd₂O₃) are 144.42, 135.70, and 158.76 MPa, respectively. Additionally, the maximum displacement of the fuel’s outer surface for the FAs of

UO₂, (UO₂ + Er₂O₃), and (UO₂ + Gd₂O₃) was 0.145, 0.130, and 0.172 mm. The solid structure results indicate the safe operation of the three investigated FAs because the maximum von Mises stress acting on the fuel materials was less than the yield stress of UO₂. Furthermore, although the displacement of the fuel outer surface is greater than the

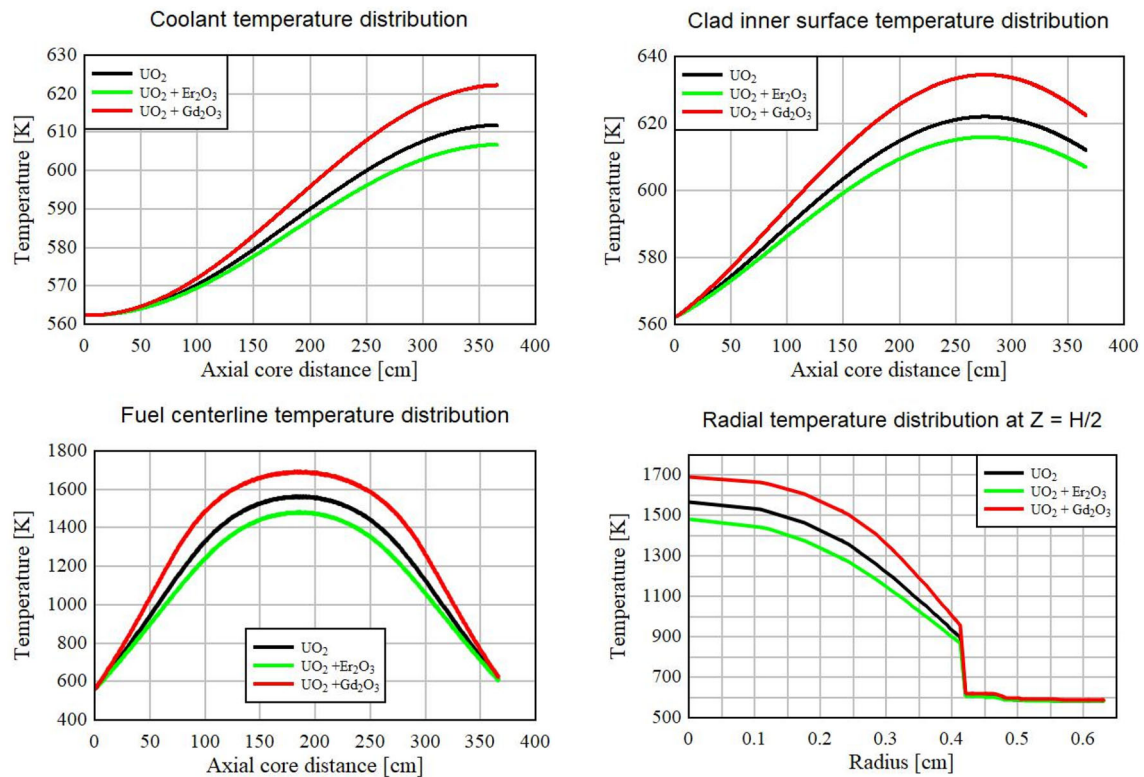


Fig. 7 (Color online) Radial and axial temperature distributions for the investigated FAs of UO_2 , $\text{UO}_2 + \text{Er}_2\text{O}_3$, and $\text{UO}_2 + \text{Gd}_2\text{O}_3$

thickness of the He gap, PCCI will not occur because the maximum clad temperature in the three investigated FAs is smaller than the safety limit of 1135 K. Er_2O_3 provided the best solid structure performance compared to UO_2 and the suggested FA ($\text{UO}_2 + \text{Gd}_2\text{O}_3$).

The results of the TH and solid structure parameters confirmed our findings from neutronic calculations, in which Er_2O_3 gave the best performance and now provided the best and safest TH and solid structure performances relative to Gd_2O_3 in the case of UO_2 . Therefore, Er_2O_3 is applied to the investigated thorium-based fuel types in the following section.

3.3 Effect of Er_2O_3 on thorium-based fuel types

After investigating the TH and solid structure performances of the traditional FA with Er_2O_3 and Gd_2O_3 , the former proved to be the best IFBA for application to thorium-based fuels. Figure 10 presents the distribution of the radial and axial PPFs for the examined FAs ($\text{UO}_2 + \text{Er}_2\text{O}_3$, $(^{232}\text{Th}, ^{235}\text{U})\text{O}_2 + \text{Er}_2\text{O}_3$, and $(^{232}\text{Th}, ^{233}\text{U})\text{O}_2 + \text{Er}_2\text{O}_3$).

As shown in Table 6, the use of Er_2O_3 reduces the total PPF for $(^{232}\text{Th}, ^{235}\text{U})\text{O}_2$ from 1.695 to 1.663 and reduces the total PPF for $(^{232}\text{Th}, ^{233}\text{U})\text{O}_2$ from 1.552 to 1.469. This reduction in the total PPF reflects the effective role of Er_2O_3 in enhancing the neutronic performance, as discussed in the first annex of this work, and the performance of the TH and solid structure. The main objective of this section is to reduce the maximum fuel and cladding temperatures and increase the value of MDNBR by applying Er_2O_3 to the two thorium-based fuel types and the standard fuel material.

3.3.1 Thermal hydraulic performance

In this section, the gain in TH performance after applying Er_2O_3 to the investigated thorium-based FAs of UO_2 , $(^{232}\text{Th}, ^{235}\text{U})\text{O}_2 + \text{Er}_2\text{O}_3$, and $(^{232}\text{Th}, ^{233}\text{U})\text{O}_2 + \text{Er}_2\text{O}_3$ is illustrated. As shown in Fig. 11, for UO_2 , the maximum fuel temperature decreased from 1565.21 K to 1481.99 K, the maximum clad temperature decreased from 622.07 K to 615.95 K, and the MDNBR

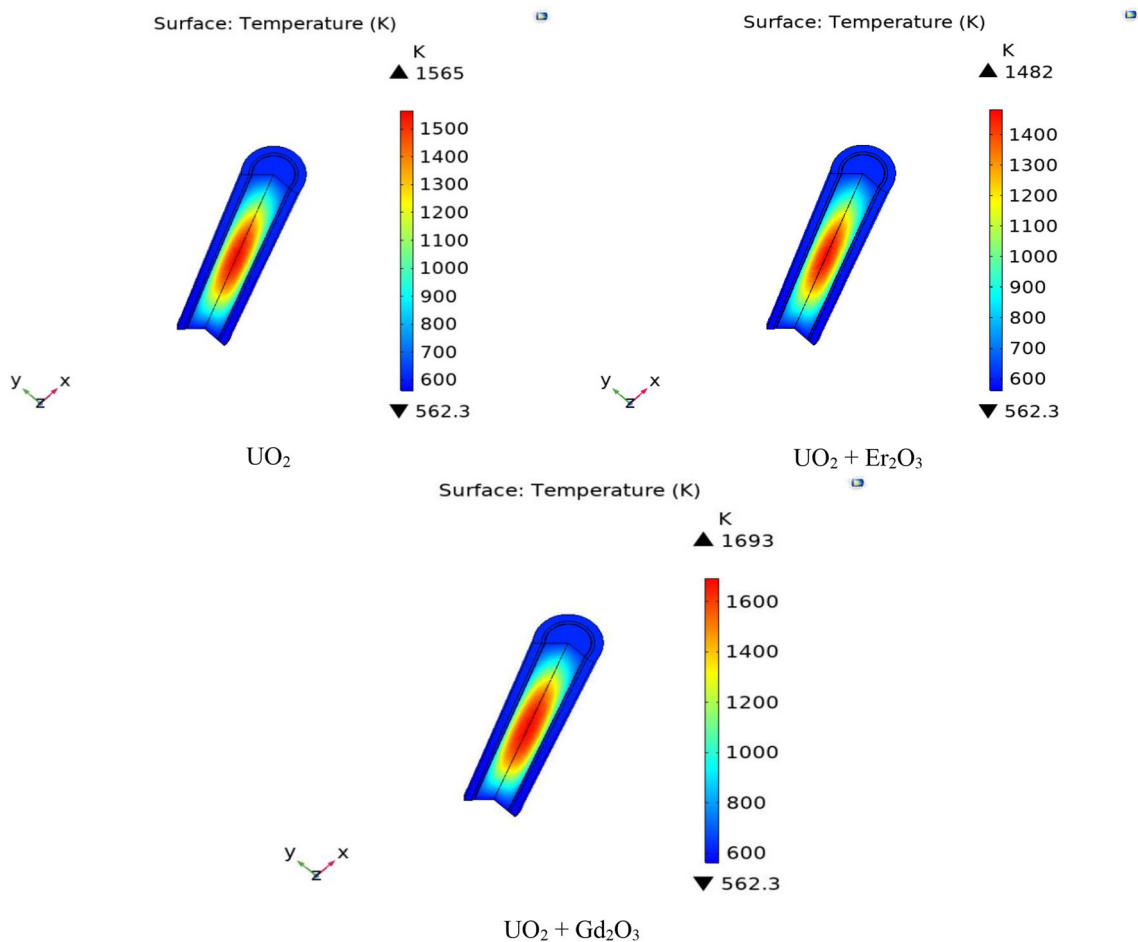


Fig. 8 (Color online) 3D temperature distributions for UO_2 , $(UO_2 + Er_2O_3)$, and $(UO_2 + Gd_2O_3)$

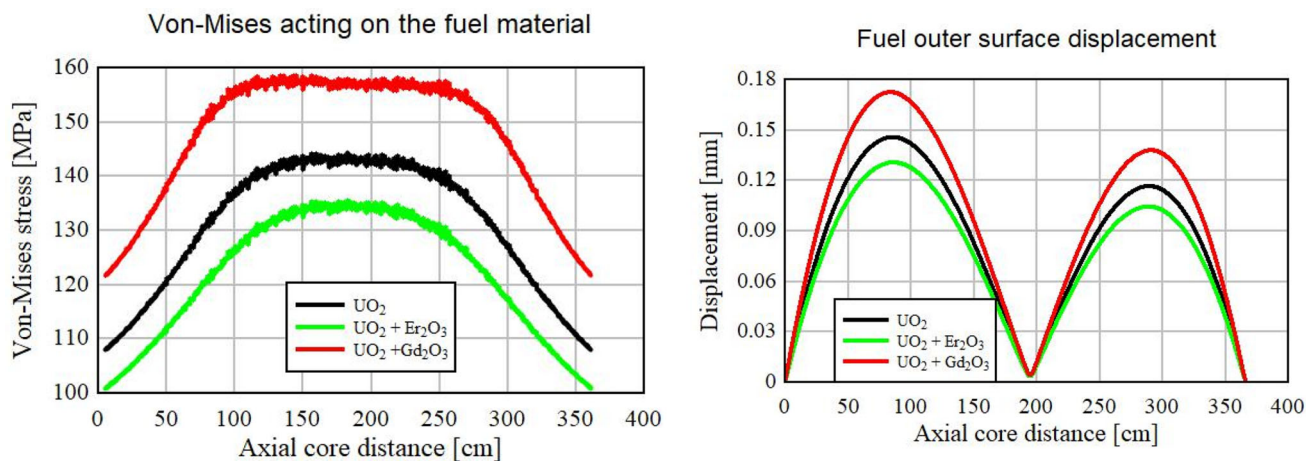


Fig. 9 (Color online) Results of the main solid structure parameters for the investigated FAs of UO_2 , $(UO_2 + Er_2O_3)$, and $(UO_2 + Gd_2O_3)$

9	18		33	42		57	66	
1.047	1.081		1.080	1.104		0.901	1.085	
8	17	25	32	41	48	56	65	72
1.033	1.031	0.889	1.033	1.052	1.100	1.056	1.057	1.084
7	16	24	31	40	47	55	64	71
1.046	1.061	1.079	1.043	0.880	1.095	1.071	1.053	0.899
6	15		30	39		54	63	
1.058	1.099		1.112	1.106		1.086	1.086	
5	14	23	29	38	46	53	62	70
1.053	1.056	0.918	1.125	1.113	1.097	0.877	1.037	1.094
4	13	22		37	45	52	61	69
1.054	1.061	1.100		1.113	1.104	1.033	1.036	1.076
3	12	21	28	36		51	60	
1.042	1.049	1.073	1.096	0.926		1.072	0.890	
2	11	20	27	35	44	50	59	68
1.040	1.049	1.052	1.060	1.052	1.100	1.061	1.043	1.077
1	10	19	26	34	43	49	58	67
1.042	1.048	1.049	1.055	1.046	1.065	1.039	1.042	1.047

UO₂+Er₂O₃

9	18		33	42		57	66	
1.023	1.056		1.059	1.073		0.915	1.066	
8	17	25	32	41	48	56	65	72
1.026	1.026	0.907	1.019	1.029	1.078	1.039	1.045	1.080
7	16	24	31	40	47	55	64	71
1.032	1.049	1.061	1.029	0.895	1.071	1.054	1.043	0.917
6	15		30	39		54	63	
1.038	1.067		1.092	1.079		1.085	1.075	
5	14	23	29	38	46	53	62	70
1.024	1.029	0.935	1.096	1.082	1.083	0.889	1.029	1.078
4	13	22		37	45	52	61	69
1.023	1.034	1.077		1.090	1.091	1.036	1.025	1.060
3	12	21	28	36		51	60	
1.022	1.020	1.041	1.066	0.935		1.060	0.901	
2	11	20	27	35	44	50	59	68
1.014	1.015	1.024	1.028	1.035	1.080	1.037	1.017	1.055
1	10	19	26	34	43	49	58	67
1.019	1.014	1.019	1.019	1.023	1.032	1.031	1.021	1.022

(²³²Th,²³³U) O₂+Er₂O₃

9	18		33	42		57	66	
1.060	1.091		1.092	1.113		0.918	1.104	
8	17	25	32	41	48	56	65	72
1.062	1.056	0.905	1.045	1.059	1.104	1.068	1.082	1.111
7	16	24	31	40	47	55	64	71
1.062	1.069	1.092	1.051	0.894	1.117	1.080	1.074	0.922
6	15		30	39		54	63	
1.073	1.115		1.132	1.125		1.119	1.120	
5	14	23	29	38	46	53	62	70
1.068	1.086	0.951	1.147	1.123	1.127	0.893	1.063	1.119
4	13	22		37	45	52	61	69
1.057	1.075	1.132		1.155	1.134	1.062	1.054	1.098
3	12	21	28	36		51	60	
1.060	1.063	1.092	1.119	0.953		1.103	0.912	
2	11	20	27	35	44	50	59	68
1.065	1.061	1.067	1.079	1.071	1.120	1.082	1.048	1.101
1	10	19	26	34	43	49	58	67
1.057	1.059	1.054	1.069	1.063	1.067	1.060	1.046	1.063

(Th,²³⁵U) O₂+Er₂O₃

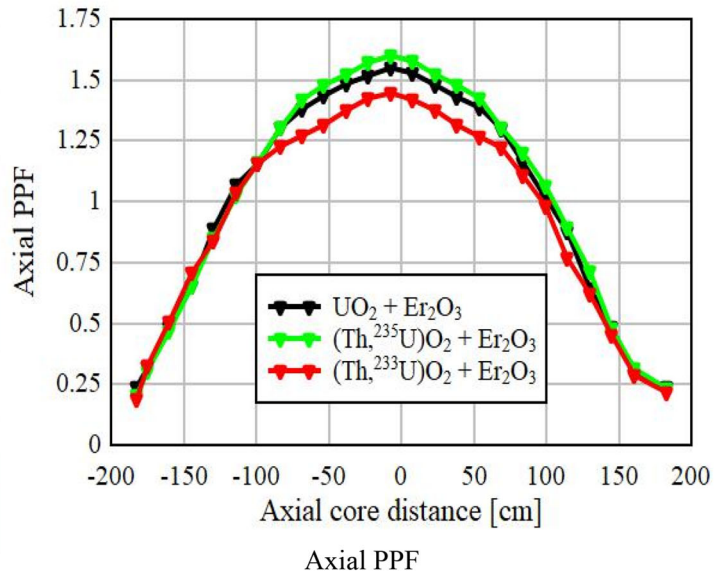


Fig. 10 (Color online) Radial and axial PPF distributions for the investigated FAs (UO₂ + Er₂O₃), (²³²Th, ²³⁵U) O₂ + Er₂O₃, and (²³²Th, ²³³U) O₂ + Er₂O₃

Table 6 Maximum radial PPF, maximum axial PPF, and the total PPF for the investigated thorium-based FAs of (²³²Th, ²³⁵U) O₂ + Er₂O₃ and (²³²Th, ²³³U) O₂ + Er₂O₃

Assembly	FA with (²³² Th, ²³⁵ U) O ₂ + Er ₂ O ₃	FA with (²³² Th, ²³³ U) O ₂ + Er ₂ O ₃
Max radial PPF	1.155	1.096
Max axial PPF	1.600	1.490
Total PPF	1.663	1.469

increased from 1.767 to 1.847. For (²³²Th, ²³⁵U) O₂, the maximum fuel, clad temperatures, and the MDNBR are 1497.56 K, 620.20 K, and 1.765, respectively. These values are reduced to 1474.70 K, 619.01 K, and 1.787, respectively, after applying Er₂O₃. For (²³²Th, ²³³U)O₂, the maximum fuel temperature decreased from 1403.49 K to 1352.20 K, the maximum clad temperature decreased from 615.26 K to 612.51 K, and the MDNBR increased from 1.8615 to 1.919. Figure 12 presents the 3D temperature distributions for the three examined FAs (UO₂, (²³²Th, ²³⁵U) O₂ + Er₂O₃, and (²³²Th, ²³³U)O₂ + Er₂O₃).

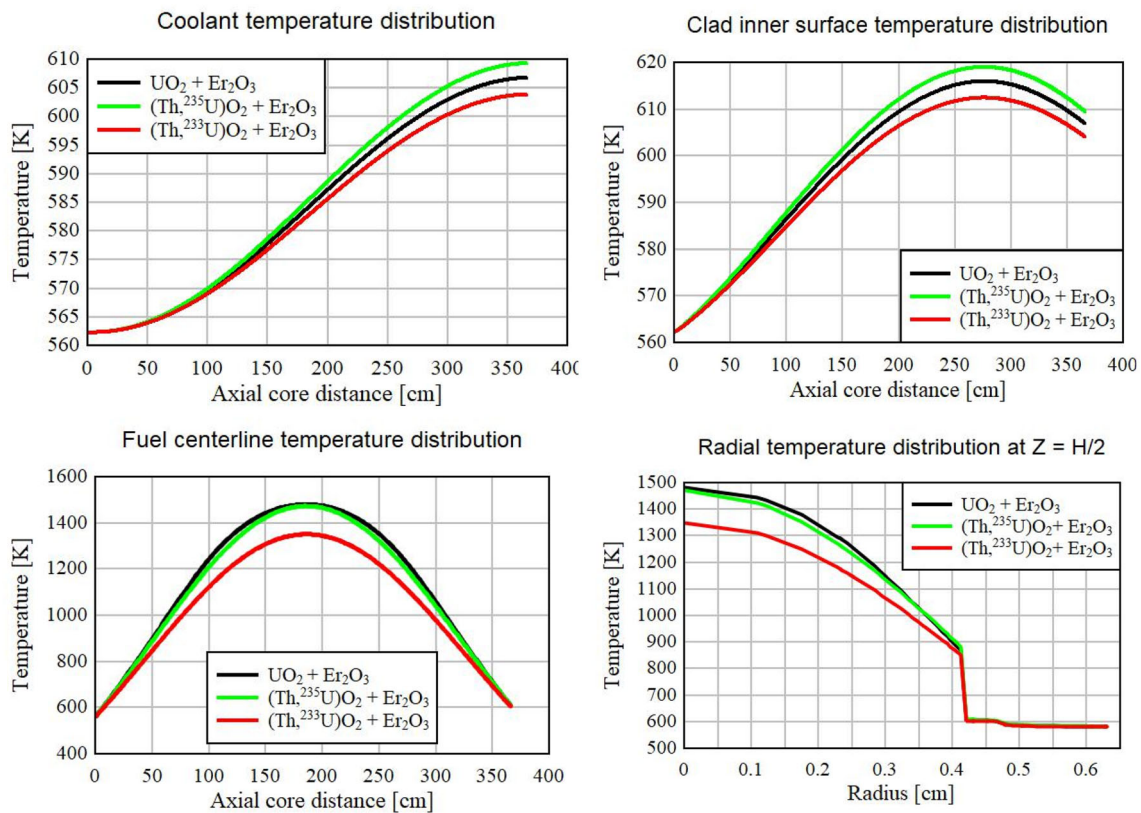


Fig. 11 (Color online) Radial and axial temperature distributions in the investigated FAs of $\text{UO}_2 + \text{Er}_2\text{O}_3$, $(^{232}\text{Th}, ^{235}\text{U})\text{O}_2 + \text{Er}_2\text{O}_3$, and $(^{232}\text{Th}, ^{233}\text{U})\text{O}_2 + \text{Er}_2\text{O}_3$

3.3.2 Solid structure performance

The gain in solid structure performance after applying Er_2O_3 to the investigated FAs ($\text{UO}_2 + \text{Er}_2\text{O}_3$, $(^{232}\text{Th}, ^{235}\text{U})\text{O}_2 + \text{Er}_2\text{O}_3$, and $(^{232}\text{Th}, ^{233}\text{U})\text{O}_2 + \text{Er}_2\text{O}_3$) is illustrated in Fig. 13. For UO_2 , the von Mises stress and the displacement of the fuel's outer surface decreased after applying Er_2O_3 from 144.42 MPa and 0.145 mm to 135.70 MPa and 0.130 mm, respectively. For $(^{232}\text{Th}, ^{235}\text{U})\text{O}_2$, the von Mises stress operating on the fuel material decreased from 111.06 to 109.12 MPa and the fuel outer surface displacement decreased from 0.098 to 0.095 mm. Finally, the greatest von Mises stress, acting on the $(^{232}\text{Th}, ^{233}\text{U})\text{O}_2$, decreased from 103.08 to 98.74 MPa and the displacement of its fuel's outer surface decreased from 0.089 to 0.084 mm after applying Er_2O_3 .

Table 7 presents a summary of the results obtained from neutronic, TH, and solid structure analyses. This illustrates the effectiveness of each type of fuel and proves that the

thorium-based fuels are a very good alternative to UO_2 . There are several reasons for the difference between the results of the TH and solid structure parameters of the investigated FAs, firstly, the difference in the values of the various thermophysical properties that are used in the solution of the heat generation partial differential equation, such as thermal conductivity (K), heat capacity at constant pressure (C_p), density (ρ), and heat source (total PPF), as illustrated in Table 3. Additionally, the difference in the solid structure properties of the investigated FAs is based on the variation in Young's modulus (E), Poisson's ratio (ν), and thermal expansion coefficient (α). The dominant factors that strongly affect the TH and solid structure results are the heat source value (total PPF) and the thermal expansion coefficient, assuming that the remaining factors are almost the same for all the investigated fuel materials. The main turbulence properties are assumed to be the same for all investigated fuel assemblies, such as the coolant mass flow rate of 16,720 kg/s, coolant inlet pressure of

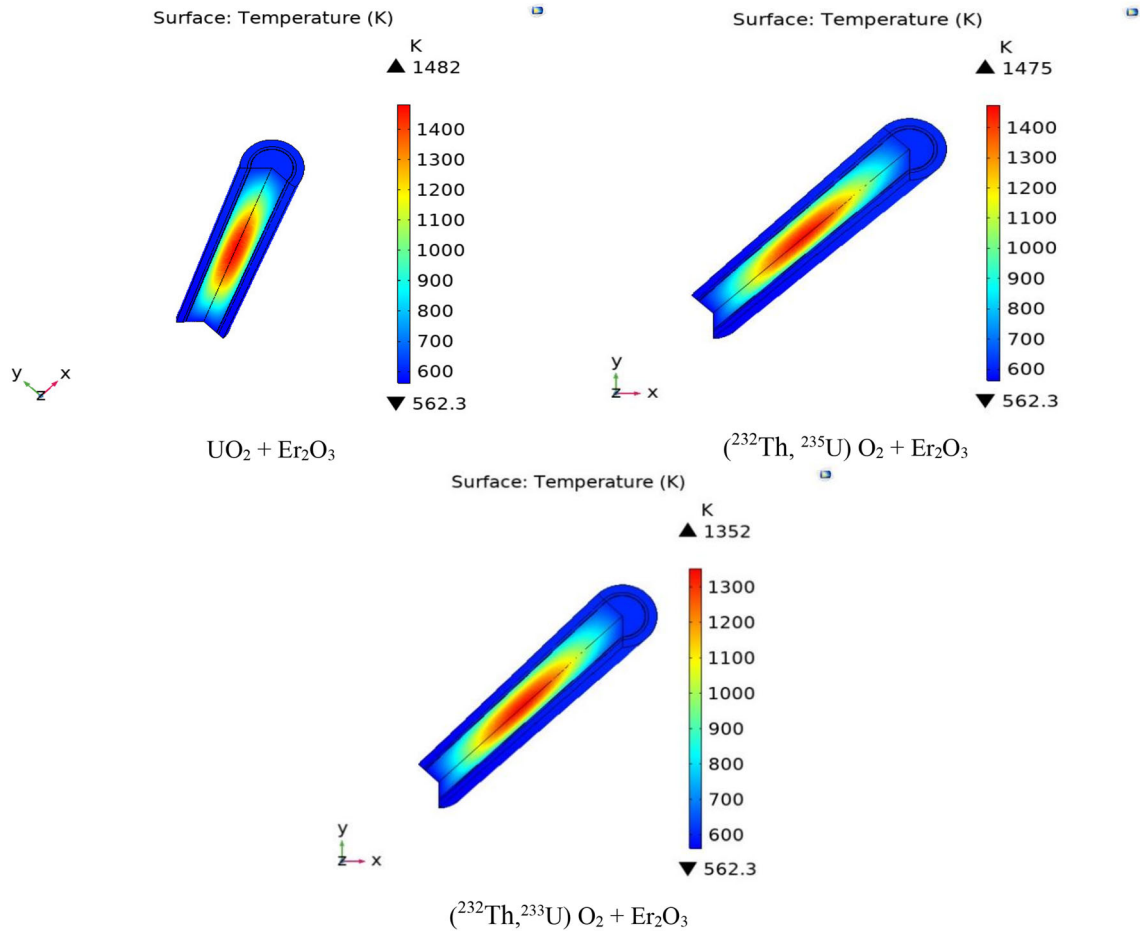


Fig. 12 (Color online) 3D temperature distribution for $\text{UO}_2 + \text{Er}_2\text{O}_3$, $(^{232}\text{Th}, ^{235}\text{U})\text{O}_2 + \text{Er}_2\text{O}_3$, and $(^{232}\text{Th}, ^{233}\text{U})\text{O}_2 + \text{Er}_2\text{O}_3$

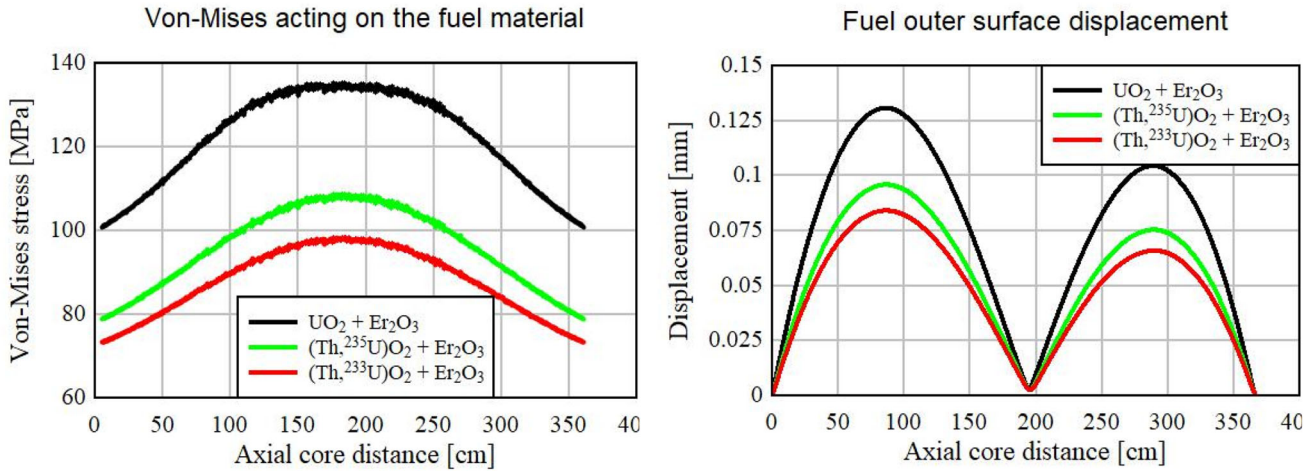


Fig. 13 (Color online) Results of the main solid structure parameters for the investigated FAs of $\text{UO}_2 + \text{Er}_2\text{O}_3$, $(^{232}\text{Th}, ^{235}\text{U})\text{O}_2 + \text{Er}_2\text{O}_3$, and $(^{232}\text{Th}, ^{233}\text{U})\text{O}_2 + \text{Er}_2\text{O}_3$

Table 7 Results of the main neutronic, TH, and solid structure parameters for the investigated FAs of $\text{UO}_2 + \text{Er}_2\text{O}_3$, $(^{232}\text{Th}, ^{235}\text{U})\text{O}_2 + \text{Er}_2\text{O}_3$, and $(^{232}\text{Th}, ^{233}\text{U})\text{O}_2 + \text{Er}_2\text{O}_3$

Physics	Parameters	$\text{UO}_2 + \text{Er}_2\text{O}_3$	$(^{232}\text{Th}, ^{235}\text{U})\text{O}_2 + 2\% \text{Er}_2\text{O}_3$	$(^{232}\text{Th}, ^{233}\text{U})\text{O}_2 + 2\% \text{Er}_2\text{O}_3$	Safety limits
Neutronic	Max radial PPF	1.125	1.155	1.096	–
	Max axial PPF	1.552	1.600	1.490	–
	Total PPF	1.571	1.663	1.469	–
	Actinide inventory	Top	Medium	Least	–
	Non-actinide inventory	Top	Medium	Least	–
TH	Max fuel temperature (K)	1481.99	1474.70	1352.20	For UO_2 , it must not be greater than solidus point 2873 K in LWRs [13] For (U, Th) O_2 , it must not be greater than the melting point of 3500 K
	Max clad temperature (K)	615.95	619.01	612.51	It should be less than melting point 2123 K [13]
	MDNBR	1.847	1.787	1.919	It should be greater than 1.75 [13]
Solid structure	Max von Mises stress (MPa)	135.70	109.12	98.74	For UO_2 , it must be less than 170 MPa [20] For ThO_2 , it must be less than 175 MPa [25, 26]
	Max displacement of the fuel outer surface (mm)	0.130	0.095	0.084	It should not be greater than the thickness of the He gap of 0.08 mm [17]

15.41 MPa, turbulence model ($K-\varepsilon$), and wall condition (no-slip).

4 Conclusion

From the neutronic perspective, the results show that the use of $(^{232}\text{Th}, ^{235}\text{U})\text{O}_2$ and $(^{232}\text{Th}, ^{233}\text{U})\text{O}_2$ reduced the actinides and non-actinides nuclide inventory, which decreased the radioactivity of the spent fuel during the storage step.

From the TH perspective, the high melting point of the thorium $(^{232}\text{Th}, ^{235}\text{U})\text{O}_2$ and $(^{232}\text{Th}, ^{233}\text{U})\text{O}_2$ is one of its essential thermophysical properties. Additionally, the maximum fuel and cladding temperatures for the $(\text{Th}, ^{235}\text{U})\text{O}_2$ and $(^{232}\text{Th}, ^{233}\text{U})\text{O}_2$ are lower than those for the standard fuel (UO_2), while the MDNBR values of $(^{232}\text{Th}, ^{235}\text{U})\text{O}_2$ and $(^{232}\text{Th}, ^{233}\text{U})\text{O}_2$ were greater than those of UO_2 .

From the solid structure perspective, owing to the superiority of the solid structure properties of $(^{232}\text{Th}, ^{235}\text{U})\text{O}_2$ and $(^{232}\text{Th}, ^{233}\text{U})\text{O}_2$ over that of UO_2 , the maximum von Mises stress operating on the fuel and cladding materials and the displacement of the fuel's outer surface are less than that of UO_2 . Thus, it can be concluded from the neutronic, TH, and solid structure perspectives that $(^{232}\text{Th}, ^{235}\text{U})\text{O}_2$ and $(^{232}\text{Th}, ^{233}\text{U})\text{O}_2$ are good alternatives for the traditional fuel material UO_2 .

Authors' contributions All authors contributed to the study conception and design. Material preparation, data collection, and analysis were performed by Mohamed Y.M. Mohsen, Mohamed A.E. Abdel-Rahman, and A. Abdelghafar Galahom. The first draft of the manuscript was written by Mohamed Y.M. Mohsen, and all authors commented on previous versions of the manuscript. All authors read and approved the final manuscript.

References

- L.G.G. Fonseca, M. Hedberg, L. Huan et al., Application of SPS in the fabrication of UN and (U, Th)N pellets from microspheres. *J. Nucl. Mater.* **536**, 152181 (2020). <https://doi.org/10.1016/j.jnucmat.2020.152181>
- M.Y.M. Mohsen, M.A.E. Abdel-Rahman, A.A. Galahom, Integrated analysis of VVER-1000 fuel assembly fueled with accident tolerant fuel (ATF) materials. *Ann. Nucl. Energy* **159**, 108330 (2021). <https://doi.org/10.1016/j.anucene.2021.108330>
- A.A. Galahom, M.Y.M. Mohsen, N. Amrani, Explore the possible advantages of using thorium-based fuel in a pressurized water reactor (PWR) part 1: neutronic analysis. *Nucl. Eng. Technol.* (2021). <https://doi.org/10.1016/j.net.2021.07.019>
- F. Faghihi, S.M. Mirvakili, Burn up calculations for the Iranian miniature reactor: a reliable and safe research reactor. *Nucl. Eng. Des.* **239**, 1000–1009 (2009). <https://doi.org/10.1016/j.nucengdes.2009.01.014>
- Y. Lu, Y. Yang, P. Zhang, Thermodynamic properties and structural stability of thorium dioxide. *J. Phys. Condens. Matter* **24**, 225801 (2012). <https://doi.org/10.1088/0953-8984/24/22/225801>
- H. Muta, Y. Murakami, M. Uno et al., Thermophysical properties of $\text{Th}_{1-x}\text{U}_x\text{O}_2$ pellets prepared by spark plasma sintering technique. *J. Nucl. Sci. Technol.* **50**, 181–187 (2013). <https://doi.org/10.1080/00223131.2013.757468>

7. A.A. Galahom, Minimization of the fission product waste by using thorium based fuel instead of uranium dioxide. *Nucl. Eng. Des.* **314**, 165–172 (2017). <https://doi.org/10.1016/j.nucengdes.2017.01.024>
8. E.H. Ugurua, S.F. Abdulsani, M.U. Khandaker et al., Investigation on the effect of ^{238}U replacement with ^{232}Th in small modular reactor (SMR) fuel matrix. *Prog. Nucl. Energy* **118**, 103108 (2020). <https://doi.org/10.1016/j.pnucene.2019.103108>
9. S.M. Mirvakili, Z. Gholamzadeh, S.A.H. Fegghi, Computational analysis of neutronic effects of ThO₂ rods loaded in CANDU 6 fuel assemblies. *Nucl. Sci. Tech.* **27**, 79 (2016). <https://doi.org/10.1007/s41365-016-0101-y>
10. J. Al Zain, O. El Hajjaji, T. El Bardouni et al., Neutronic and burn-up calculations of the (ThO₂–UO₂) pin cell benchmark using DRAGON5 and MCNP6.2 codes with ENDF/B-VIII.0 nuclear data library. *Int. J. Energy Res.* **45**, 11538–11551 (2021). <https://doi.org/10.1002/er.6460>
11. X. Zhao, D. Cui, X. Cai et al., Analysis of Th-U breeding capability for an accelerator-driven subcritical molten salt reactor. *Nucl. Sci. Tech.* **29**, 121 (2018). <https://doi.org/10.1007/s41365-018-0448-3>
12. D.P. Daroca, S. Jaroszewicz, A.M. Llois et al., Phonon spectrum, mechanical and thermophysical properties of thorium carbide. *J. Nucl. Mater.* **437**, 135–138 (2013). <https://doi.org/10.1016/j.jnucmat.2013.01.350>
13. A.E. Shields, D. Santos-Carballal, N.H. de Leeuw, A density functional theory study of uranium-doped thoria and uranium adatoms on the major surfaces of thorium dioxide. *J. Nucl. Mater.* **473**, 99–111 (2016). <https://doi.org/10.1016/j.jnucmat.2016.02.009>
14. A.E. Shields, S.E.R. Hernandez, N.H. de Leeuw, Theoretical analysis of uranium-doped thorium dioxide: introduction of a thoria force field with explicit polarization. *AIP Adv.* **5**, 087118 (2015). <https://doi.org/10.1063/1.4928438>
15. G. McKinney, *MCNPX User's Manual*. Version 2 (7) (2011)
16. A.A. Galahom, Improving the neutronic characteristics of a boiling water reactor by using uranium zirconium hydride fuel instead of uranium dioxide fuel. *Nucl. Eng. Technol.* **48**, 751–757 (2020). <https://doi.org/10.1016/j.net.2016.01.003>
17. N.E. Todreas, M.S. Kazimi, *Nuclear Systems I: Thermal Hydraulic Fundamentals* (Hemisphere Publishing Co., New York, 1990). ISBN: 0891169350
18. M.Y.M. Mohsen, M.S. Hassan, M. Aziz et al., Investigating the neutronic, thermal-hydraulic, and solid mechanics analysis for AP-1000 nuclear reactor. *Energy Sources Part A Recovery Util. Environ. Eff.* **1**, 5 (2021). <https://doi.org/10.1080/15567036.2021.1912215>
19. IAEA, *Thermophysical Properties of Materials for Nuclear Engineering: A Tutorial and Collection of Data* (Vienna, 2009)
20. V. Haase, H. Keller-Rudek, L. Manes et al., *U Uranium-Supplement Volume C5 Uranium Dioxide, UO₂, Physical Properties* (Springer, Berlin, 1986). <https://doi.org/10.1007/978-3-662-10719-5>
21. K. Geelhood, W.G. Luscher, *Material Property Correlations: Comparisons Between FRAPCON-4.0, FRAPTRAN-2.0, and MATPRO* (2015). <https://doi.org/10.2172/1030897>
22. A.K. Sengupta, T. Jarvis, M.R. Nair et al., *Thermal Diffusivity and Thermal Conductivity of (Th, U)O FUELS*. INDIA (2000). <https://doi.org/10.1016/j.jnucmat.2018.01.014>
23. F. Faghihi, S.M. Mirvakili, S.S. Arshi et al., Neutronics and sub-channel thermal-hydraulics analysis of the Iranian VVER-1000 fuel bundle. *Prog. Nucl. Energy* **87**, 39–46 (2016). <https://doi.org/10.1016/j.pnucene.2015.10.020>
24. A.A. Galahom, Investigation of different burnable absorbers effects on the neutronic characteristics of PWR assembly. *Ann. Nucl. Energy* **94**, 22–31 (2016). <https://doi.org/10.1016/j.anucene.2016.02.025>
25. S. Peterson, R.E. Adams, D.A. Douglas Jr., *Properties of Thorium, Its Alloys and Its Compounds* (International Atomic Energy Agency (IAEA): IAEA, 1966)
26. R.A. Wolfe, S.F. Kaufman, *Mechanical Properties of Oxide Fuels* (LSBR/LWB DEVELOPMENT PROGRAM), United States 1967-01-01. <https://www.osti.gov/biblio/4511674>